

# SC-TauPath: A Structural Connectivity Attribution Framework for Mapping Tau Propagation Pathways in Alzheimer’s Disease

Jing Zhang<sup>1</sup>, Norman Scheel<sup>2</sup>, Minheng Chen<sup>1</sup>, Tong Chen<sup>1</sup>, Yanjun Lyu<sup>1</sup>,  
David C. Zhu<sup>2</sup>, Rong Zhang<sup>3</sup>, and Dajiang Zhu<sup>1</sup>(✉)

<sup>1</sup> University of Texas at Arlington, Arlington, TX, USA  
{jxz7537,mxc2442,txc5603,yx19168}@mavs.uta.edu, dajiang.zhu@uta.edu

<sup>2</sup> Michigan State University, East Lansing, MI, USA  
scheelno@msu.edu, david.zhu@einsteinmed.edu

<sup>3</sup> University of Texas Southwestern Medical Center, Dallas, TX, USA  
rongzhang@texashealth.org

**Abstract.** Understanding how structural connections are associated with tau propagation in Alzheimer’s disease (AD) remains a central open question, yet existing computational models either rely heavily on biophysical assumptions or lack neurobiologically interpretable pathway maps. We present **SC-TauPath**, a structural connectivity (SC) attribution framework that maps tau propagation pathways from in vivo neuroimaging data. SC-TauPath combines a Network Diffusion Model (NDM)-augmented multilayer perceptron with gradient  $\times$  input attribution to score each SC edge’s contribution to tau prediction, then translates these attribution scores into multi-scale pathway maps (backbone edges, high-traffic routes, and hub ROIs), which validates established Braak staging anatomy. Applied to 234 ADNI participants with paired DTI SC and <sup>18</sup>F-Flortaucipir PET, SC-TauPath achieves strong cross-validated tau prediction and yields attribution-based pathway maps consistent with established Braak staging anatomy, demonstrating that SC encode spatially specific information about regional tau distribution in AD.

**Keywords:** AD · tau propagation · structural connectivity

## 1 Introduction

A defining feature of Alzheimer’s disease is the hierarchical spread of hyperphosphorylated tau protein through the cortex, following a stereotyped anatomical trajectory described by [3]. Specifically, tau pathology initiates in the entorhinal cortex (Braak stages I–II), advances into limbic regions including the hippocampus (stages III–IV), and eventually invades widespread neocortex (stages V–VI). Increasing evidence from preclinical models and in vivo <sup>18</sup>F-Flortaucipir PET imaging indicates that this progression is not random: tau accumulation follows patterns consistent with transsynaptic spread along white-matter connections, with structurally connected regions showing correlated pathological burden [8,

15, 16, 7]. A central and still-open question therefore is: *which specific structural connections are most strongly associated with regional tau burden, and can we read these pathways from neuroimaging data?*

Physics-based Network Diffusion Models (NDMs) have made important contributions by formalizing tau spread as heat-equation diffusion on the structural connectome [8]. More recent work has systematically evaluated alternative connectome constructions within this framework to improve population-level modeling of tau and neurodegeneration [18, 17, 9]. Yet NDMs carry inherent limitations: they assume exponential decay dynamics, a single global diffusivity constant, and fixed seed regions, which restrict their flexibility. Consequently, they cannot identify which individual structural edges are most strongly associated with propagation, nor do they provide a ranked, subject-level map of propagation pathways. Data-driven deep learning methods, in contrast, can capture individual variability, but the learned representations often function as black boxes rather than provide interpretable pathway maps.

To address these, we introduce **SC-TauPath**, a structural connectivity (SC) attribution framework designed specifically to map tau propagation pathways from in vivo imaging. SC-TauPath includes three tightly coupled parts: **(i) NDM-augmented MLP regression.** A NDM first generates a biophysically informed diffusion prior per subject, which is then combined with edge-level and node-level SC features as input to a multilayer perceptron trained to predict individual tau SUVR profiles. **(ii) Gradient  $\times$  input edge attribution.** For each test subject in every fold, we compute gradient  $\times$  input saliency [1] with respect to SC edge features, yielding an attribution score that measures the actual influence of each connection to the predicted tau spatial distribution. **(iii) Multi-scale pathway analysis.** Attribution scores are integrated into a weighted graph to derive four complementary and interpretable representations: backbone edges, high-traffic routes, multi-hop propagation pathways, and hub ROIs. Applied to 234 ADNI participants, SC-TauPath not only accurately captures the population-level tau distribution and individual-level deviations, but also derives SC-based pathway maps and reveal a temporal-frontal dissociation between pathological epicenters and structurally central relay hubs.

## 2 Methodology

### 2.1 Participants and Data Processing

We analyzed 234 participants (122 CN, 83 MCI, and 29 AD) from the Alzheimer’s Disease Neuroimaging Initiative (ADNI), each with tau PET ( $^{18}\text{F}$ -Flortaucipir), diffusion MRI (DTI), and structural MRI (T1-weighted) scans available. Regional tau PET standardized uptake value ratios (SUVRs) were obtained following the standard pipeline in [14]. The PET image was first co-registered to the subject’s T1 by SPM, subsequently, the T1 was normalized to the rrAD420 template - an anatomical atlas optimized for older adult populations - and the resulting transformation was applied to the PET image [11, 10]. SUVRs were

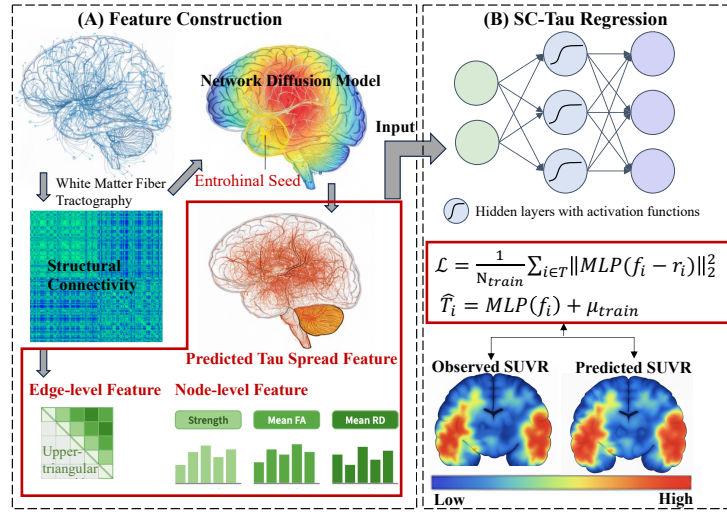


Fig. 1. Overview of the proposed framework with two main parts.

computed voxel-wise using cerebellar gray matter as the reference region. Regional tau PET SUVRs were then extracted using the Brainnetome atlas [5], yielding a 246-dimensional SUVR vector per subject.

SC was derived following the standardized preprocessing pipeline described in [20, 19]. Briefly, skull stripping was applied to both normalized T1 and DTI images, after which DTI was registered to T1 space using FSL. The brain was parcellated into 246 regions of interest (ROIs) using the Brainnetome atlas, a fine-grained whole-brain parcellation grounded in structural connectivity architecture. Tractography yielded a subject-specific  $246 \times 246$  connectivity matrix, whose edge-level features encoding pairwise structural connectivity strength by fiber count. Regional node-level features were additionally extracted, including node strength, mean fractional anisotropy (FA), and mean radial diffusivity (RD) (See (Fig 1(A)). All features were z-score normalized prior to model input.

## 2.2 Network Architecture

**Network Diffusion Model.** To incorporate a biophysically informed prior of tau propagation, we employed a Network Diffusion Model (NDM) defined on each subject’s structural connectome (See (Fig 1(A)). Pathology diffusion was modeled using the heat equation on the graph Laplacian:

$$\frac{d\mathbf{x}(t)}{dt} = -\beta\mathbf{H}\mathbf{x}(t), \quad (1)$$

where  $\mathbf{x}(t) \in \mathbb{R}^N$  denotes the regional pathology distribution at model time  $t$ ,  $\beta$  is the diffusivity constant, and  $\mathbf{H}$  is the normalized graph Laplacian derived from the subject-specific SC matrix. The closed-form solution is given by:

$$\mathbf{x}(t) = e^{-\beta \mathbf{H}t} \mathbf{x}_0 = \mathbf{U} e^{-\beta \mathbf{\Lambda}t} \mathbf{U}^\top \mathbf{x}_0, \quad (2)$$

where  $\mathbf{H} = \mathbf{U}\mathbf{\Lambda}\mathbf{U}^\top$  is the eigendecomposition of  $\mathbf{H}$ , with  $\mathbf{\Lambda} = \text{diag}(\lambda_1, \dots, \lambda_N)$  and orthonormal eigenvectors  $\mathbf{U}$ . This decomposition was precomputed per subject to enable efficient evaluation across the parameter grid.

*Initial Condition.* The diffusion process was seeded at bilateral entorhinal cortex, consistent with canonical Braak stage I/II origins of tau pathology. The initial condition vector  $\mathbf{x}_0$  was defined as:

$$x_0(i) = \begin{cases} \frac{1}{|\mathcal{S}|}, & i \in \mathcal{S} \\ 0, & \text{otherwise} \end{cases} \quad (3)$$

where  $\mathcal{S}$  is the seed region set, followed by normalization such that  $\|\mathbf{x}_0\|_1 = 1$ .

*Parameter Optimization.* NDM parameters were optimized globally within each cross-validation fold using training subjects only. To allow flexible integration between the NDM prediction and the empirical group-mean pattern, a scalar mixing coefficient  $\gamma$  was introduced, forming the blended prediction:

$$\hat{\boldsymbol{\tau}}_i^{\text{NDM}}(\beta, t, \gamma) = \gamma \mathbf{x}_i(t; \beta) + (1 - \gamma) \boldsymbol{\mu}_{\text{train}}, \quad (4)$$

where  $\mathbf{x}_i(t; \beta) \in \mathbb{R}^{246}$  is the NDM-predicted tau distribution for subject  $i$  and  $\boldsymbol{\mu}_{\text{train}} \in \mathbb{R}^{246}$  is the training-set mean tau profile. The parameters  $(\beta, t, \gamma)$  were jointly optimized by minimizing the mean squared error (MSE):

$$(\beta^*, t^*, \gamma^*) = \arg \min_{\beta, t, \gamma} \frac{1}{N_{\text{train}}} \sum_{i=1}^{N_{\text{train}}} \|\hat{\boldsymbol{\tau}}_i^{\text{NDM}}(\beta, t, \gamma) - \boldsymbol{\tau}_i\|_2^2, \quad (5)$$

where  $\boldsymbol{\tau}_i \in \mathbb{R}^{246}$  is the observed tau SUVR vector for subject  $i$ . The resulting subject-specific NDM output  $\mathbf{x}_i(t^*; \beta^*)$  was appended as additional feature.

**SC-to-Tau Regression.** A multilayer perceptron (MLP) was trained to predict individual regional tau profiles from a combined feature vector (See (Fig 1(B))). For each subject  $i$ , the input feature vector was constructed as:

$$\mathbf{f}_i = \left[ \text{vec}(\mathbf{A}_i^\Delta); \mathbf{z}_i^{\text{node}}; \mathbf{x}_i(t^*; \beta^*) \right] \in \mathbb{R}^D, \quad (6)$$

where  $\text{vec}(\mathbf{A}_i^\Delta) \in \mathbb{R}^{30135}$  contains the upper-triangular edge-level SC features,  $\mathbf{z}_i^{\text{node}} \in \mathbb{R}^{738}$  stacks the three node-level SC features across all ROIs, and  $\mathbf{x}_i(t^*; \beta^*) \in \mathbb{R}^{246}$  is the NDM-derived feature.

*Residual Target Formulation.* To capture subject-specific deviations beyond population-level patterns, we adopted a residual prediction strategy. For each cross-validation fold, the training-set mean tau profile was first computed as:

$$\boldsymbol{\mu}_{\text{train}} = \frac{1}{N_{\text{train}}} \sum_{j \in \mathcal{T}} \boldsymbol{\tau}_j, \quad (7)$$

where  $\boldsymbol{\tau}_j \in \mathbb{R}^{246}$  is the observed tau SUVR vector for subject  $j$  and  $\mathcal{T}$  denotes the training index set. The individual residual target was then defined as  $\mathbf{r}_i = \boldsymbol{\tau}_i - \boldsymbol{\mu}_{\text{train}}$ . The MLP was trained to approximate  $\mathbf{r}_i$  by minimizing the MSE:

$$\mathcal{L} = \frac{1}{N_{\text{train}}} \sum_{i \in \mathcal{T}} \|\text{MLP}(\mathbf{f}_i) - \mathbf{r}_i\|_2^2. \quad (8)$$

At inference, the tau prediction was recovered by  $\hat{\boldsymbol{\tau}}_i = \text{MLP}(\mathbf{f}_i) + \boldsymbol{\mu}_{\text{train}}$ .

### 3 Experiments and Results

#### 3.1 Experimental Setup

The MLP architecture and training hyperparameters were selected via grid search. The final configuration consisted of two fully connected hidden layers with 256 and 128 units respectively, each followed by ReLU activation and dropout regularization (rate = 0.2), optimized using the Adam optimizer with a learning rate of  $10^{-3}$  and weight decay of  $10^{-4}$ . Training was conducted with a batch size of 64 for up to 640 epochs, with early stopping applied. The parameters  $(\beta, t, \gamma)$  were jointly optimized via grid search over  $\beta \in \{0.05, 0.1, 0.2, 0.5, 1.0\}$ ,  $t \in \{0.5, 1.0, 2.0, 4.0, 8.0\}$ ,  $\gamma \in [0, 1]$ , and the selected parameters were consistent across the majority of folds ( $\beta = 0.05$ ,  $t = 8.0$ ,  $\gamma = 0.4$ ; 4 of 5 folds). The best checkpoint was selected by minimum validation MSE.

Model generalizability was assessed via stratified 5-fold cross-validation. At each fold, subjects were partitioned into training (80%), validation (10%), and test (10%) sets. All preprocessing steps, including NDM parameter optimization, feature normalization, and MLP training, were performed exclusively on training-fold data to prevent leakage. Test-set predictions across all five folds were assembled into an out-of-fold (OOF) prediction matrix  $\hat{\mathbf{T}} \in \mathbb{R}^{234 \times 246}$  covering all subjects. Prediction performance was evaluated using per-subject Pearson and Spearman rank correlations between  $\hat{\boldsymbol{\tau}}_i$  and  $\boldsymbol{\tau}_i$ , averaged across subjects, in both absolute tau space and residual space.

#### 3.2 Results

##### SC Captures Population-Common and Subject-Specific Tau Pattern

Across 5-fold cross-validation, our method achieved a mean Pearson correlation of  $r = 0.778 \pm 0.018$  and Spearman correlation  $\rho = 0.753 \pm 0.019$  between predicted and observed tau SUVR profiles across brain regions, with  $R^2 = 0.241 \pm 0.082$ , indicating our approaches captured the dominant common spatial pattern of tau deposition. The performance is summarized in Table 1. To isolate the model’s capacity to predict subject-level deviations, we evaluated performance in the residual space - defined by subtracting the training-set mean tau profile prior to scoring. In this space, performance decreased substantially ( $r = 0.123 \pm 0.053$ ;  $\rho = 0.128 \pm 0.048$ ;  $R^2 = 0.110 \pm 0.071$ ; See Table 1), suggesting that SC encodes weak yet detectable signal of inter-subject tau variability beyond the shared spatial pattern. The ablation study in Table 1 reveals a complementary relationship between NDM features and MLP-based regression.

**Table 1.** Cross-validated model performance and comparison (mean  $\pm$  SD across 5 folds).

Space	Method	Pearson $r$	Spearman $\rho$	$R^2$
Full Tau Profile	NDM only	$0.756 \pm 0.013$	$0.748 \pm 0.012$	$0.206 \pm 0.076$
	MLP only	$0.703 \pm 0.018$	$0.702 \pm 0.018$	$0.148 \pm 0.012$
	NDM + MLP (ours)	<b><math>0.778 \pm 0.018</math></b>	<b><math>0.753 \pm 0.019</math></b>	<b><math>0.241 \pm 0.082</math></b>
Residual Space	NDM only	$-0.009 \pm 0.003$	$-0.005 \pm 0.008$	$-0.003 \pm 0.006$
	MLP only	$0.116 \pm 0.013$	$0.125 \pm 0.033$	$-0.134 \pm 0.003$
	NDM + MLP (ours)	<b><math>0.193 \pm 0.053</math></b>	<b><math>0.158 \pm 0.048</math></b>	<b><math>0.110 \pm 0.071</math></b>

**Backbone Edge Identification** We first examined the specific structural edges that most strongly associated with tau propagation, referred to as *backbone edges*, and visualize them in Figure 2(a). To further characterize the network topology of these backbone edges, we computed *high-traffic edges*, defined as the edges most frequently traversed by shortest paths between all pairs of high-degree nodes, and visualize them in Figure 2(b). Three findings are highlighted: **First**, the STG $\leftrightarrow$ FuG connection (right superior temporal gyrus to left fusiform gyrus) was identified as both a backbone edge (ranking #2) and a high-traffic edge (ranking #4, See Figure 2(a) and (b), dashed black), and both ROIs rank among the top-30 hubs, indicating that this connection serves as a key structural bridge linking structurally dominant and topologically central regions within the tau spread network. **Second**, the top-ranked high-traffic edge involves the middle temporal gyrus, the top-5 hubs, further indicating the centrality of this region in tau propagation (Figure 2(b) and (d), dashed green). **Third**, the left middle frontal gyrus (MFG) appears in both backbone edges and high-traffic edges (Figure 2(a) and (b), dashed red). This region corresponds to the dorsolateral prefrontal cortex, a key association area involved in later Braak stages (V–VI) of tau pathology [2, 12].

**Backbone Pathways Identification** To characterize the global routing architecture of tau propagation, we identified *backbone pathways* - the information highways connecting top hub ROIs - by computing shortest paths between all pairs of top hubs using  $1/\mathcal{I}_k$  as the edge distance, where higher saliency corresponds to shorter effective distance. The left MFG emerged as a recurring waypoint, appearing in three distinct backbone pathways (Figure 2(c), dashed yellow). From a SC perspective, the region maintains strong white matter projections to both parietal and temporal cortices [4], positioning it as a key bridging region positioned between posterior cortical hubs and prefrontal cortex, whose high attribution scores are consistent with its role in later-stage tau involvement, consistent with the late neocortical spread characteristic of Braak stages V–VI.

**Hub ROI Identification** Hub scores quantify each ROI’s aggregate contribution to tau propagation by summing the saliency-derived importance of all incident edges, visualizing in Figure 2(d). The highest-scoring hub, the precuneus,

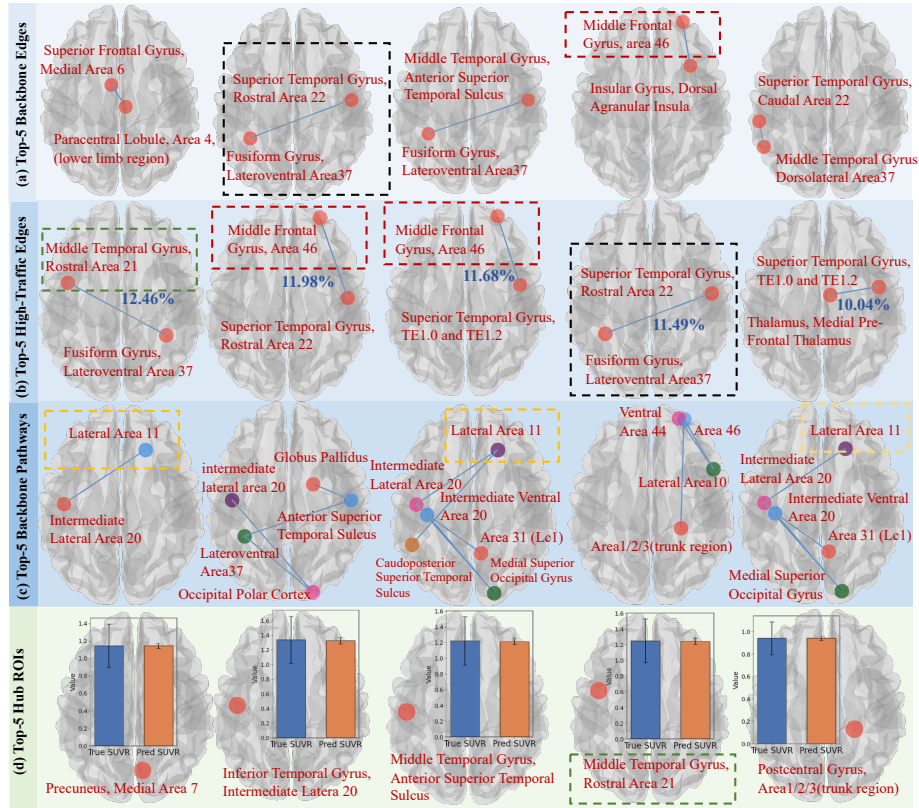


**Fig. 2.** Top-5 (a) Saliency-Ranked Backbone Edges, (b) High-Traffic Routing Edges, (c) Backbone Multi-hop Pathways, and (d) Degree-weighted Hub ROIs.

is a core node of the default mode network (DMN) and a characteristic region of neocortical tau involvement in later Braak stages (V–VI) [13, 6], suggesting that the SC scaffold captured by our model aligns with tau propagation trajectories observed in vivo. The inferior and middle temporal gyri, ranking among the top attribution hubs, correspond to Braak stage III–IV neocortical regions, consistent with their role as regions structurally positioned between medial temporal areas and broader cortex, where tau accumulation is observed to escalate in intermediate Braak stages [13].

**Regional Heterogeneity in Individual-Level Deviations** To examine individual variability, we analyzed residual distributions in two representative ROIs exhibiting maximal structural-pathological contrast (Figure 3). We selected *left fusiform gyrus, lateral ventral area 37 (FuG\_L)*, a temporal pathological epicenter ranking #2/246 in AD-specific residual excess, and *right middle frontal gyrus, area 46 (MFG\_R)*, a frontal structural hub with highest

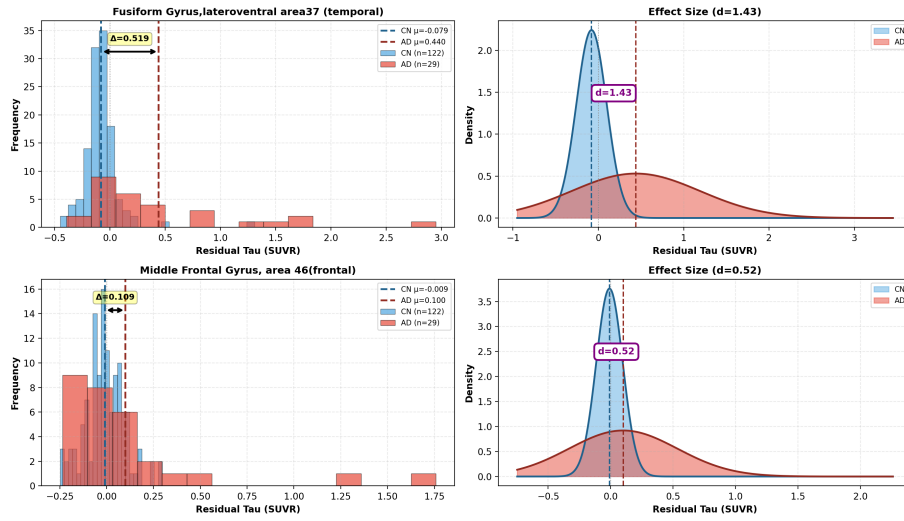


**Fig. 3.** Temporal-frontal dissociation in AD-specific residual tau.

backbone degree but ranking only #154/246 in AD-excess. Both ROIs participate in high-traffic propagation routes (See Fig 2).

Figure 3 reveals significant differences in individual-level residual patterns between these regions. The FuG\_L (Top panel of Fig 3) exhibited very large effect size (Cohen’s  $d = 1.43$ ), with AD participants showing mean residuals of  $+0.44$  SUVR compared to near-zero CN residuals ( $-0.08$  SUVR). Critically, AD participants exhibited **4.2-fold higher** residual variance ( $\sigma = 0.75$ ) than CN ( $\sigma = 0.18$ ), reflecting substantial individual heterogeneity in pathological burden at this site. In stark contrast, the MFG\_R (Bottom panel of Fig 3) showed only medium effect size ( $d = 0.52$ ) with minimal residuals (AD :  $+0.10$  SUVR vs. CN:  $-0.01$  SUVR) and lower variance inflation (AD:  $\sigma = 0.43$ ; CN:  $\sigma = 0.11$ , 3.9-fold). This **4.4-fold difference** in mean AD-specific residuals ( $+0.44$  vs.  $+0.10$ ) indicates that tau accumulation in temporal regions exceeds what can be attributed to SC alone, whereas residual burden in frontal hubs is minimal and largely consistent with SC-predicted tau distribution. This pattern suggests that temporal cortex shows tau accumulation beyond SC predictions, while frontal hub tau levels are more closely aligned with SC-based expectations.

## 4 Conclusion

We introduced SC-TauPath, an attribution framework that enables the SC-to-tau prediction model interpretable by mapping tau propagation pathways. By applying gradient-based attribution, we identified structural edges and hub regions that contribute most strongly to tau spatial distribution. The results align with Braak staging patterns and canonical association hubs, supporting the hy-

pothesis that SC is associated with the spatial patterning of tau accumulation. SC-TauPath shifts the focus from predictive performance alone to mechanistic interpretability, offering a strategy to interpret network-based disease models and may facilitate future studies of pathological spread in neurodegenerative disorders. Future work will extend the framework to longitudinal data, graph neural network architectures, and multimodal inputs including functional connectivity.

## References

1. Ancona, M., Ceolini, E., Öztireli, C., Gross, M.: Towards better understanding of gradient-based attribution methods for deep neural networks. arXiv preprint arXiv:1711.06104 (2017)
2. Braak, H., Alafuzoff, I., Arzberger, T., Kretschmar, H., Del Tredici, K.: Staging of alzheimer disease-associated neurofibrillary pathology using paraffin sections and immunocytochemistry. *Acta neuropathologica* **112**(4), 389–404 (2006)
3. Braak, H., Braak, E.: Neuropathological staging of alzheimer-related changes. *Acta neuropathologica* **82**(4), 239–259 (1991)
4. Briggs, R.G., Lin, Y.H., Dadario, N.B., Kim, S.J., Young, I.M., Bai, M.Y., Dhannaraj, V., Fonseka, R.D., Hormovas, J., Tanglay, O., et al.: Anatomy and white matter connections of the middle frontal gyrus. *World Neurosurgery* **150**, e520–e529 (2021)
5. Fan, L., Li, H., Zhuo, J., Zhang, Y., Wang, J., Chen, L., Yang, Z., Chu, C., Xie, S., Laird, A.R., et al.: The human brainnetome atlas: a new brain atlas based on connectional architecture. *Cerebral cortex* **26**(8), 3508–3526 (2016)
6. Hansson, O., Grothe, M.J., Strandberg, T.O., Ohlsson, T., Hägerström, D., Jögi, J., Smith, R., Schöll, M.: Tau pathology distribution in alzheimer’s disease corresponds differentially to cognition-relevant functional brain networks. *Frontiers in neuroscience* **11**, 167 (2017)
7. Huang, Y., Dan, T., Kim, W.H., Wu, G.: Uncovering cortical pathways of prion-like pathology spreading in alzheimer’s disease by neural optimal mass transport. In: *International Conference on Medical Image Computing and Computer-Assisted Intervention*. pp. 498–508. Springer (2024)
8. Raj, A., Tora, V., Gao, X., Cho, H., Choi, J.Y., Ryu, Y.H., Lyoo, C.H., Franchi, B.: Combined model of aggregation and network diffusion recapitulates alzheimer’s regional tau-positron emission tomography. *Brain connectivity* **11**(8), 624–638 (2021)
9. Sandell, R., Torok, J., Nagaragan, S., Ranasinghe, K.G., Ma, D., Raj, A.: Integrating event-based and network diffusion models to predict individual tau progression in alzheimer’s disease. *Alzheimer’s & Dementia* **21**, e107645 (2025)
10. Scheel, N., Fernandez, Z., Baker, J., Yanev, P., Keller, J.N., Binder, E.F., Vidoni, E.D., Burns, J.M., Stowe, A.M., Kerwin, D.R., et al.: A functional resting-state network atlas based on 420 older adults with hypertension. *bioRxiv* pp. 2025–11 (2025)
11. Scheel, N., Keller, J.N., Binder, E.F., Vidoni, E.D., Burns, J.M., Stowe, A.M., Kerwin, D.R., Vongpatanasin, W., Cullum, M., Zhang, R., et al.: Introducing rrad420, an anatomical template and multi-modal atlas for older adults. *Alzheimer’s & Dementia* **18**, e068920 (2022)
12. Schilling, L.P., Zimmer, E.R., Shin, M., Leuzy, A., Pascoal, T.A., Benedet, A.L., Borelli, W.V., Palmieri, A., Gauthier, S., Rosa-Neto, P.: Imaging alzheimer’s disease pathophysiology with pet. *Dementia & neuropsychologia* **10**(02), 79–90 (2016)

13. Schöll, M., Lockhart, S.N., Schonhaut, D.R., O’Neil, J.P., Janabi, M., Ossenkoppele, R., Baker, S.L., Vogel, J.W., Faria, J., Schwimmer, H.D., et al.: Pet imaging of tau deposition in the aging human brain. *Neuron* **89**(5), 971–982 (2016)
14. Villemagne, V.L., Leuzy, A., Bohorquez, S.S., Bullich, S., Shimada, H., Rowe, C.C., Bourgeat, P., Lopresti, B., Huang, K., Krishnadas, N., et al.: Centaur: toward a universal scale and masks for standardizing tau imaging studies. *Alzheimer’s & Dementia: Diagnosis, Assessment & Disease Monitoring* **15**(3), e12454 (2023)
15. Watanabe, H., Bagarinao, E., Yokoi, T., Yamaguchi, H., Ishigaki, S., Mausuda, M., Katsuno, M., Sobue, G.: Tau accumulation and network breakdown in alzheimer’s disease. *Tau biology* pp. 231–240 (2020)
16. Yang, F., Chowdhury, S.R., Jacobs, H.I., Johnson, K.A., Dutta, J.: A longitudinal model for tau aggregation in alzheimer’s disease based on structural connectivity. In: *International Conference on Information Processing in Medical Imaging*. pp. 384–393. Springer (2019)
17. Yang, F., Chowdhury, S.R., Jacobs, H.I., Sepulcre, J., Wedeen, V.J., Johnson, K.A., Dutta, J.: Longitudinal predictive modeling of tau progression along the structural connectome. *Neuroimage* **237**, 118126 (2021)
18. Zhang, J., Yang, D., He, W., Wu, G., Chen, M.: A network-guided reaction-diffusion model of at [n] biomarkers in alzheimer’s disease. In: *2020 IEEE 20th International Conference on Bioinformatics and Bioengineering (BIBE)*. pp. 222–229. IEEE (2020)
19. Zhang, L., Wang, L., Gao, J., Risacher, S.L., Yan, J., Li, G., Liu, T., Zhu, D., Initiative, A.D.N., et al.: Deep fusion of brain structure-function in mild cognitive impairment. *Medical image analysis* **72**, 102082 (2021)
20. Zhang, L., Wang, L., Zhu, D., Initiative, A.D.N., et al.: Predicting brain structural network using functional connectivity. *Medical image analysis* **79**, 102463 (2022)